

# Nonlinear Electrochemical Impedance Spectroscopy as a Novel Approach to Identify an Electrochemical Reaction Mechanism at Electrode-Electrolyte Interface

*Pachimatla Rajesh*

Department of Chemical Engineering, Sri Sivasubramaniya Nadar College of Engineering - Kalavakkam, Chennai 603110, India  
E-mail: [pachimatlar@ssn.edu.in](mailto:pachimatlar@ssn.edu.in)

*Received:* 19 January 2022 / *Accepted:* 26 February 2022 / *Published:* 5 April 2022

---

The ability of the nonlinear electrochemical impedance spectroscopy (NLEIS) technique to differentiate the reaction mechanisms was investigated. Cu electrodeposition from acidic CuSO<sub>4</sub> solution is considered as a case study. NLEIS response, i.e., the signal at fundamental and higher harmonics, was recorded using a custom-built experimental setup. A numerical framework is proposed to calculate the polarisation and NLEIS response of a reaction mechanism while incorporating both kinetics and mass transfer effects. Three candidate reaction mechanisms with adsorbed intermediates were evaluated to model the Cu electrodeposition process. A comparison of the model predicted, and experimental results show that higher harmonic response along with fundamental data can be used for better model discrimination and identify the exact reaction mechanism at the interface of an electrochemical system.

---

**Keywords:** Nonlinear Impedance, polarization, kinetics, mass transfer, Cu electrodeposition

## 1. INTRODUCTION

Electrochemical impedance spectroscopy (EIS) is a versatile technique widely used to investigate electrochemical processes [1-5]. It employs small-amplitude perturbations and is limited to the linear response of the system. Electrochemical systems are inherently nonlinear, and the nonlinearity can be probed by applying large amplitude perturbations and analysing the response at fundamental as well as higher harmonics. This emerging technique can be considered as an extended version of EIS and is known as nonlinear EIS (NLEIS) [6-13]. In this work, the term ‘NLEIS’ indicates signal at the fundamental frequency as well as higher harmonics. EIS has been employed to identify the detailed mechanism of electrochemical reactions as well as mass transfer effects [13-20]. There are relatively fewer publications on using large amplitude perturbations for mechanistic analysis and they are

summarized here. Xu and Riley studied the response of double-layer capacitance and faradaic processes to large sinusoidal perturbations using a stationary Au electrode in the classical  $\text{Fe}^{2+}/\text{Fe}^{3+}$  redox couple [13, 14]. Ferrocyanide oxidation kinetics and the effect of varying the electrode rotation rate and potential were studied in the framework of frequency response functions (FRF), which are computed using the Volterra series expansion [17, 18]. NLEIS can also be used to quickly identify instabilities in Ferro/Ferri redox couple [8].

The above studies are limited to simple electron transfer reactions and the analyses incorporate mass transfer effects. Often, electrochemical reactions are complex and involve multiple steps and intermediate species. Harrington illustrated a method to calculate the NLEIS response of complex reactions, assuming that the mass transfer is very rapid [19]. A theoretical analysis of methanol oxidation kinetics in direct methanol fuel cell was carried out in which the reaction mechanism was evaluated analytically by deriving the FRF up to the second-order [20]. A numerical methodology was proposed to simulate the response of multi-step reactions with adsorbed intermediates to large amplitude perturbations [21-24]. A significant limitation of these [19-24] studies is that the mass transfer was assumed to be rapid, and the results are not applicable when mass transfer plays a significant role in the overall electrochemical process. The copper electrodeposition mechanism has been widely studied [25-32] where cuprous ion ( $\text{Cu}^{1+}$ ) is considered as the adsorbed intermediate species. To the best of our knowledge, there are no reports illustrating the simulation of the NLEIS response of multi-step reactions with intermediates while incorporating mass transfer effects.

In this work, we investigate the Cu electrodeposition process in acidic sulfate solution using potentiodynamic polarization (PDP) and NLEIS technique. The electrochemical data were obtained using an NLEIS experimental setup which was established in our lab. Three candidate reaction mechanisms were evaluated, and direct numerical integration was employed to solve the governing equations. For each reaction mechanism, the parameter values were obtained by simultaneously fitting the model predicted values of PDP and NLEIS to the corresponding experimental data. The main objectives of this study are to (i) demonstrate a numerical solution methodology to simulate NLEIS response of multi-step reaction mechanisms with adsorbed intermediates while accounting for mass transfer and (ii) apply this method to analyse a real system and illustrate the potential of NLEIS framework as an effective tool to differentiate between mechanisms.

## 2. THEORETICAL FRAMEWORK

To model the Cu electrodeposition process, three reaction mechanisms, shown as pictorials in Fig. 1, were examined. The first and second reaction mechanisms are two-step processes involving one adsorbed intermediate species, viz.  $\text{Cu}_{\text{ads}}^{2+}$  and  $\text{Cu}_{\text{ads}}^{1+}$  respectively. In the third reaction mechanism,  $\text{Cu}^{2+}$  reduction occurs in three steps, and both  $\text{Cu}_{\text{ads}}^{2+}$  and  $\text{Cu}_{\text{ads}}^{1+}$  are present as adsorbed intermediate species. The following assumptions are adopted while formulating the governing equations: (i) the rate constants corresponding to the electrochemical steps vary exponentially with potential, (ii) the solution resistance is negligible, (iii) the region near the electrode can be approximated by a stationary film of thickness given by Levich equation, (iv) mass transfer occurs in the direction perpendicular to the electrode in a

boundary layer of finite thickness, and (v) Langmuir isotherm model is applicable and also the active surface area is assumed to be constant throughout the experiment.

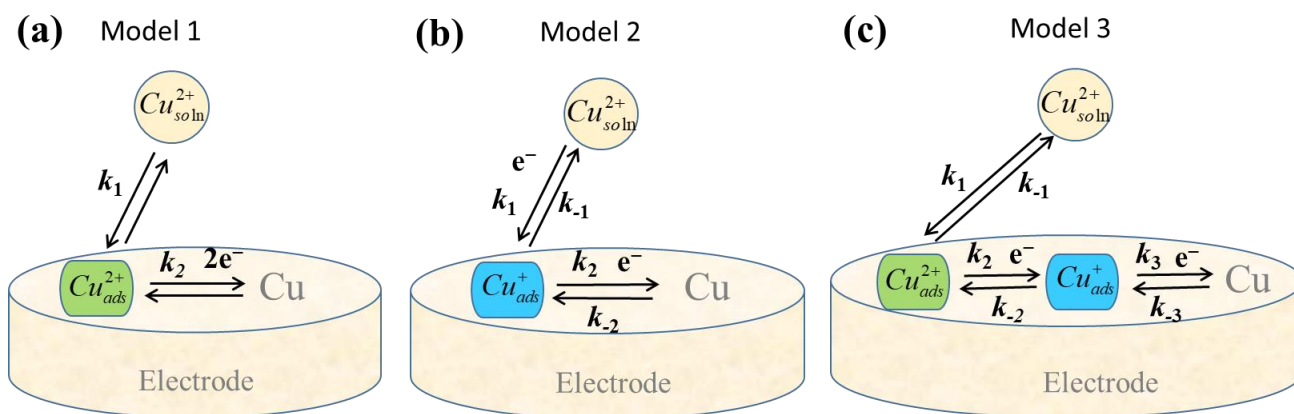


**Figure 1.** Candidate reaction mechanisms used to model Cu electrodeposition process. (a) Mechanism 1; (b) Mechanism 2; and (c) Mechanism 3.

The development of the equations to be solved is illustrated for the second mechanism here. In this reaction mechanism, cuprous ions are assumed to be reduced in two steps. Both the steps are reversible electrochemical reactions, with Cu<sub>ads</sub><sup>1+</sup> as adsorbed intermediate species on the surface. The unsteady state faradaic current can be effectively described by current – potential equation [30, 32, 33],

$$i_F(t) = nF [k_1(1-\theta_{1+})C_{0,t} - k_{-1}\theta_{1+} + k_2\theta_{1+} - k_{-2}(1-\theta_{1+})] \quad (1)$$

where  $n$  is the number of electrons transferred in the electrochemical step (in this case  $n = 1$ ),  $k_j$  ( $j = 1, -1, 2$  and  $-2$ ) is the rate constant which varies exponentially with applied potential as  $k_j = k_{j0}e^{b_j E}$ ,  $C_{0,t}$  is the concentration of the species on the surface of the electrode at any time ‘ $t$ ’,  $\theta_{1+}$  is the fractional surface coverage of Cu<sub>ads</sub><sup>1+</sup> adsorbed intermediate species and the surface coverage of bare metal sites can be denoted by  $\theta_V = (1 - \theta_{1+})$ . Here, ‘ $E$ ’ denotes electrode potential with respect to equilibrium potential across the electrode-electrolyte interface. The pre-exponents are not exactly independent and are related by the following equation [34, 35],

$$k_{-20} = \frac{k_{10}k_{20}C_{\text{bulk}}}{k_{-10}} \quad (2)$$

and this constraint was used in the analysis. The mass balance equation corresponding to reaction mechanism 2 is,

$$\Gamma \frac{d\theta_{1+}}{dt} = k_1\theta_V C_{0,t} - k_{-1}\theta_{1+} - k_2\theta_{1+} + k_{-2}\theta_V \quad (3)$$

where ‘ $\Gamma$ ’ represents the total number of sites at the monolayer surface. The boundary layer is assumed to be of uniform thickness ‘ $\delta$ ’ as given by the Levich diffusion layer thickness equation [2]. In the case of rotating disk electrode (RDE), when convection and electromigration effects are neglected, the concentration profile of species can be obtained by Fick’s second law [3, 18],

$$\frac{\partial C(x,t)}{\partial t} = D \frac{\partial^2 C(x,t)}{\partial x^2} \quad (4)$$

Here,  $D$  is the diffusion coefficient of  $\text{Cu}_{\text{sol}}^{1+}$  species. In our simulations, parameter optimization was performed while simultaneously analyzing NLEIS data acquired at two perturbation amplitudes superimposed over two dc bias values and PDP data obtained at four different electrode rotational speeds. Solution resistance and convection terms increase the complexity and stiffness in the governing equations dramatically and are neglected so that the governing equations are amenable to numerical solutions. While the solution resistance effect can be accounted for in the simulated polarization data and simulated current response at fundamental with simple algebraic equations, the same cannot be done for the current response at higher harmonics. The solution resistance was assumed to be zero in all the simulations performed to maintain consistency. At  $x = 0$ , the flux at the surface is related to the faradaic current ( $i_F$ ) as

$$D \left. \frac{\partial C}{\partial x} \right|_{x=0,t} = k_1 \theta_V C_1 - k_{-1} \theta_{1+} \quad (5)$$

At the outer edge of the boundary layer, the concentration of cuprous ion is equal to fixed bulk concentration. The boundary layer thickness ' $\delta$ ' was discretized with respect to ' $x$ ' into ' $N$ ' points, with point number 1 as surface and point number  $N$  as bulk.

For all points except number 1, Eq. (4) can be written as

$$\frac{dC_j}{dt} = D \frac{C_{j+1} + C_{j-1} - 2C_j}{(\Delta x)^2} \quad (6a)$$

At the surface,

$$\frac{dC_1}{dt} = D \frac{(C_3 - C_2)}{(\Delta x)^2} - \frac{1}{(\Delta x)} (k_1 \theta_V C_1 - k_{-1} \theta_{1+}) \quad (6b)$$

At the boundary,

$$C_N = C_{\text{bulk}} \quad (6c)$$

Equations (3) and (6) were converted to non-dimensional form [8] and were solved, along with Eq. (2), using Matlab®. The detailed steps involved in the simulation of polarization and NLEIS data are given in Appendix A, and the Matlab® program files can be obtained by contacting the corresponding author.

The unsteady state fractional surface coverage of the intermediate from the solution was substituted in Eq. (1) to calculate the unsteady state current, i.e., current as a function of time. When a sinusoidal potential of a given magnitude is applied, current values drift initially and settle after some time. While calculating the current response, sufficient time was given to obtain steady periodic values [22]. At each frequency, the unsteady state current was subjected to fast Fourier transform (FFT) to extract the current response at fundamental as well as higher harmonics. A similar procedure was adopted to solve the governing equations for reaction mechanisms 2 and 3. In this paper, the results at fundamental frequency are presented as impedance, while the harmonics (including fundamental) are presented as Bode plots of current magnitude and phase vs frequency. Since governing equations were solved directly, the results are applicable for large-amplitude perturbation as well.

### 3. EXPERIMENTAL

A three-electrode cell configuration, with a 5 mm diameter Cu working electrode, an Hg/HgSO<sub>4</sub> (in Saturated K<sub>2</sub>SO<sub>4</sub>) reference electrode and Pt mesh counter electrode, was used for conducting the experiments. The electrolyte consisted of 10 mM CuSO<sub>4</sub> and 10 mM H<sub>2</sub>SO<sub>4</sub>, and 1 M NaClO<sub>4</sub> as supporting electrolyte. When Na<sub>2</sub>SO<sub>4</sub> was used as supporting electrolyte, the Cu electrodeposition current was significantly lower at 1 M Na<sub>2</sub>SO<sub>4</sub> concentration, compared to that at 0.1 M Na<sub>2</sub>SO<sub>4</sub> concentration, indicating that adsorption of sulfate ions retard Cu electrodeposition, and hence perchlorate salt was used as supporting electrolyte. The open-circuit potential (OCP) of the Cu electrode in this solution was -0.365 V vs Hg/HgSO<sub>4</sub> and was very stable and repeatable. The OCP value is very close to the reversible potential for Cu<sup>2+</sup> electrodeposition, i.e., -0.359 V vs Hg/HgSO<sub>4</sub>. All the potentials reported in this work are with respect to OCP. The experiments were conducted at room temperature (~25 °C). The NLEIS response was acquired using a setup comprising three instruments, namely SR830 lock-in amplifier as a function generator, EC301 potentiostat and SR780 signal analyser from Stanford Research System (SRS), USA. A detailed description of the NLEIS setup to acquire accurate data for a given frequency and amplitude of perturbation is available in the literature [8, 36]. The magnitude and phase up to 3<sup>rd</sup> harmonics were recorded and analysed since higher harmonics were of low magnitude and showed poor signal to noise ratio in many of the experiments. The perturbation amplitude was varied from 20 mV to 100 mV and superimposed on two dc potentials,  $E_{dc} = -0.1$  V and -0.3 V vs OCP, and the frequency was varied from 9.984 kHz to 125 mHz, in pseudo-log space (7 frequency per decade).

### 4. RESULTS AND DISCUSSION

#### 4.1 Potentiodynamic Polarization

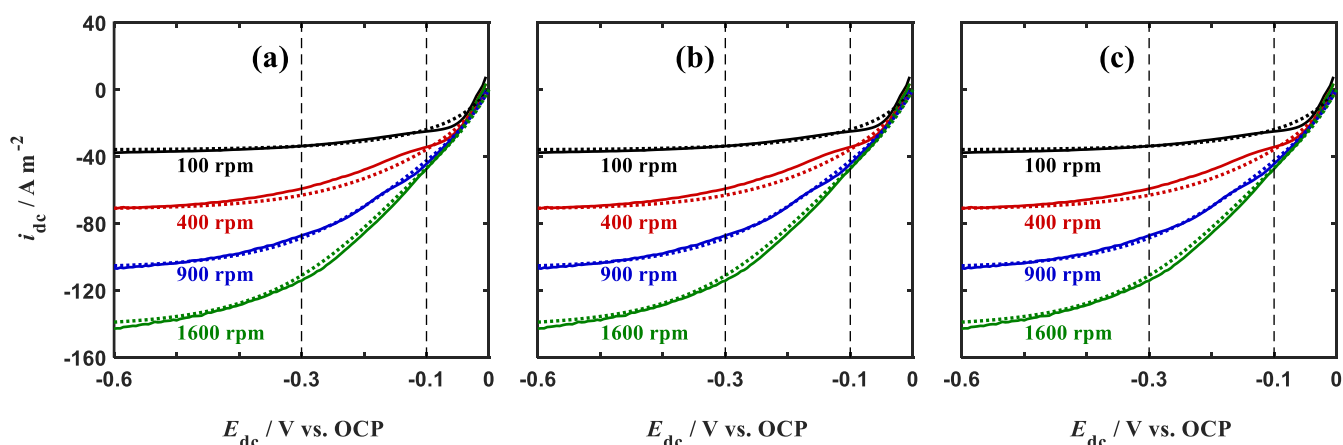


**Figure. 2** Polarization data of Cu electrodeposition on Cu, in a solution containing 10 mM CuSO<sub>4</sub> and 10 mM H<sub>2</sub>SO<sub>4</sub>, and 1 M NaClO<sub>4</sub> as supporting electrolyte, at four different electrode rotational speeds, viz. 100 (*black*), 400 (*red*), 900 (*blue*) and 1600 (*green*) rpm. Continuous lines represent the experimental data, whereas dotted lines represent the simulated data. The optimized parameters used in the simulations are listed in Table 1. PDP data simulated using (a) reaction mechanism 1; (b) reaction mechanism 2; and, (c) reaction mechanism 3.

The kinetics and mass transfer effects of an electrochemical process can be characterized by PDP studies [37, 38]. Figure 2a shows the PDP curves of Cu reduction on Cu electrode, at four-electrode rotational speeds, viz. 100, 400, 900, and 1600 rpm. The potential was swept from -0.6 V to 0 V vs OCP (with negative values representing cathodic potential) at a scan rate of 1 mV s<sup>-1</sup>. A slow scan rate was used to ensure that the PDP curve approximates the steady-state behaviour. In Fig. 2, the experimental data are shown as continuous lines, while the model results are shown as dotted lines. As expected, in the cathodic region, the Cu deposition current is limited by mass transfer and saturates at large cathodic overpotentials. Figure 2a also shows that at higher electrode rotational speeds, the limiting current values on the cathodic region are larger. It was also observed that, in the anodic region, the steady-state Cu dissolution current increases with anodic potential, and the current values remained more or less the same, irrespective of the electrode rotational speed. The steady-state current values predicted by reaction mechanisms 1, 2 and 3 matches more or less the same with experimental data, as seen in Figs. 2a, 2b and 2c. The residual sum square (RSS) was calculated by adding the square of the residuals, which are defined as the absolute value of the difference between model and experimental current values. The model current values were calculated using the parameter set given in Table 1 (*see* Multi-polarization fitting columns). Cu diffusivity was fixed in all the simulations as  $8.99 \times 10^{-6} \text{ cm}^2 \text{ s}^{-1}$ , which is close to the values proposed in the literature [28, 29, 32].

**Table 1.** Optimized parameters used for the prediction of polarization data and EIS. The diffusivity of the species ( $D_A$ ) is fixed as  $8.99 \times 10^{-6} \text{ cm}^2 \text{ s}^{-1}$  for all the simulations performed in the manuscript.

Parameters	Multi-Polarization Fitting			EIS Fitting		
	Model 1	Model 2	Model 3	Model 1	Model 2	Model 3
$k_{10}$ (Cm s <sup>-1</sup> )	$3.22 \times 10^{-1}$	$1.6 \times 10^{-3}$	$2.95 \times 10^{-1}$	$1.76 \times 10^{-1}$	$1.49 \times 10^{-3}$	$9.65 \times 10^{-2}$
$k_{-10}$ (Mol cm <sup>-2</sup> s <sup>-1</sup> )	$9.9 \times 10^{-6}$	$2.66 \times 10^{-7}$	$9.9 \times 10^{-6}$	$9.9 \times 10^{-6}$	$1.30 \times 10^{-8}$	$1.76 \times 10^{-6}$
$\alpha_1$	-	0.23	0.24	-	0.324	0.198
$k_{20}$ (Mol cm <sup>-2</sup> s <sup>-1</sup> )	$6.0 \times 10^{-8}$	$3.71 \times 10^{-8}$	$6.01 \times 10^{-8}$	$1.08 \times 10^{-7}$	$2.16 \times 10^{-8}$	$3.5 \times 10^{-8}$
$b_2$ (V <sup>-1</sup> )	9.0	-	-	0.86	-	-
$k_{-20}$ (Mol cm <sup>-2</sup> s <sup>-1</sup> )	-	-	$9.9 \times 10^{-6}$	-	-	$3.66 \times 10^{-9}$
$b_{-2}$ (V <sup>-1</sup> )	-20.9	-	-	-18.2	-	-
$\alpha_2$	-	0.827	0.79	-	0.15	0.45
$k_{30}$ (Mol cm <sup>-2</sup> s <sup>-1</sup> )	-	-	$1.64 \times 10^{-6}$	-	-	$6.69 \times 10^{-9}$
$\Gamma$ (Mol cm <sup>-2</sup> )	-	-	-	$4.18 \times 10^{-9}$	$4.99 \times 10^{-10}$	$6.25 \times 10^{-9}$
RSS	6.01	5.2	5.5	226	171	175
AIC	<b>-1295</b>	<b>-1331</b>	<b>-1312</b>	<b>48</b>	<b>38</b>	<b>43</b>

#### 4.2 Model discrimination using Akaike information criterion (AIC)

When the suitability of different models, with a different number of adjustable parameters, to describe an experimental data is examined, RSS is not the most appropriate metric for comparison.

Instead, the Akaike information criterion (AIC) is an effective technique to estimate the relative quality of different models for a given set of data. AIC score can be calculated using RSS [39] as.

$$\text{AIC} = 2k + n \times \ln\left(\frac{\text{RSS}}{n}\right) \quad (7)$$

Here  $k$  is the number of fitted parameters of the chosen model and  $n$  is the sample size. Its values are used to rank the evaluated models and the model with the lowest AIC score is considered as the best. The AIC scores corresponding to the model fits of the polarization data are listed in Table 1. Although visually all three model sets appear to match the experimental results, as shown in Fig. 2, the RSS and AIC of mechanism 2 has the least values, closely followed by the corresponding values of mechanism 3, while mechanism 1 has slightly higher RSS and AIC score. Here, the most negative value indicates the best fit by the model. Since the AIC scores for all the three mechanisms are similar, the confidence in model discrimination between these three choices, particularly between 2 and 3, is low. Next, NLEIS data was analyzed.

### 4.3 NLEIS Analysis

#### 4.3.1 Impedance data at fundamental

The unsteady state current computed from each of the reaction mechanisms is subjected to FFT, and the signal component at fundamental was used to calculate the faradaic impedance  $Z_F$ . In a linear domain, an electrochemical system can be characterized by impedance, i.e., vector ratio of potential to current, using the values at the fundamental frequency. In this method, the physicochemical parameter values were obtained by fitting the model to experimental complex impedance data. The impedance values predicted by the mechanistic analysis at the above-mentioned operating conditions are presented as complex plane plots and compared with experimental data as shown in Fig. 3. The experimental results are represented by continuous lines, whereas the simulated results are represented as open markers. The optimum parameters were found by utilizing the RSS value as the convergence criterion, which was calculated as,

$$\text{RSS} = \sum_{j=1}^M \left( \sum_{k=1}^N |Z_{\text{Exp}}(j, k) - Z_{\text{Model}}(j, k)|^2 \right) \quad (8)$$

Here  $M$  is the total number of operating conditions, viz.  $E_{\text{dc}}$  and  $E_{\text{ac0}}$  choice and  $N$  is the total number frequencies at which complex impedance data was acquired. The four operating conditions are,  $E_{\text{ac0}} = -0.02$  V with a dc bias of  $-0.1$  V and  $-0.3$  V vs OCP, and  $E_{\text{ac0}} = -0.1$  V with a dc bias of  $-0.1$  V and  $-0.3$  V vs OCP.  $Z_{\text{Exp}}(j, k)$  and  $Z_{\text{Model}}(j, k)$  are respectively the experimental and model-predicted complex impedance data at  $k^{\text{th}}$  frequency point for  $j^{\text{th}}$  operating condition. The optimized parameter sets for each model are listed in Table 1 (see EIS fitting columns).

The complex impedance data simulated by reaction mechanisms 2 and 3 matches semi-quantitatively with experimental results, whereas complex impedance data simulated by reaction mechanism 1 matches poorly with experimental results, as shown in Fig. 3.

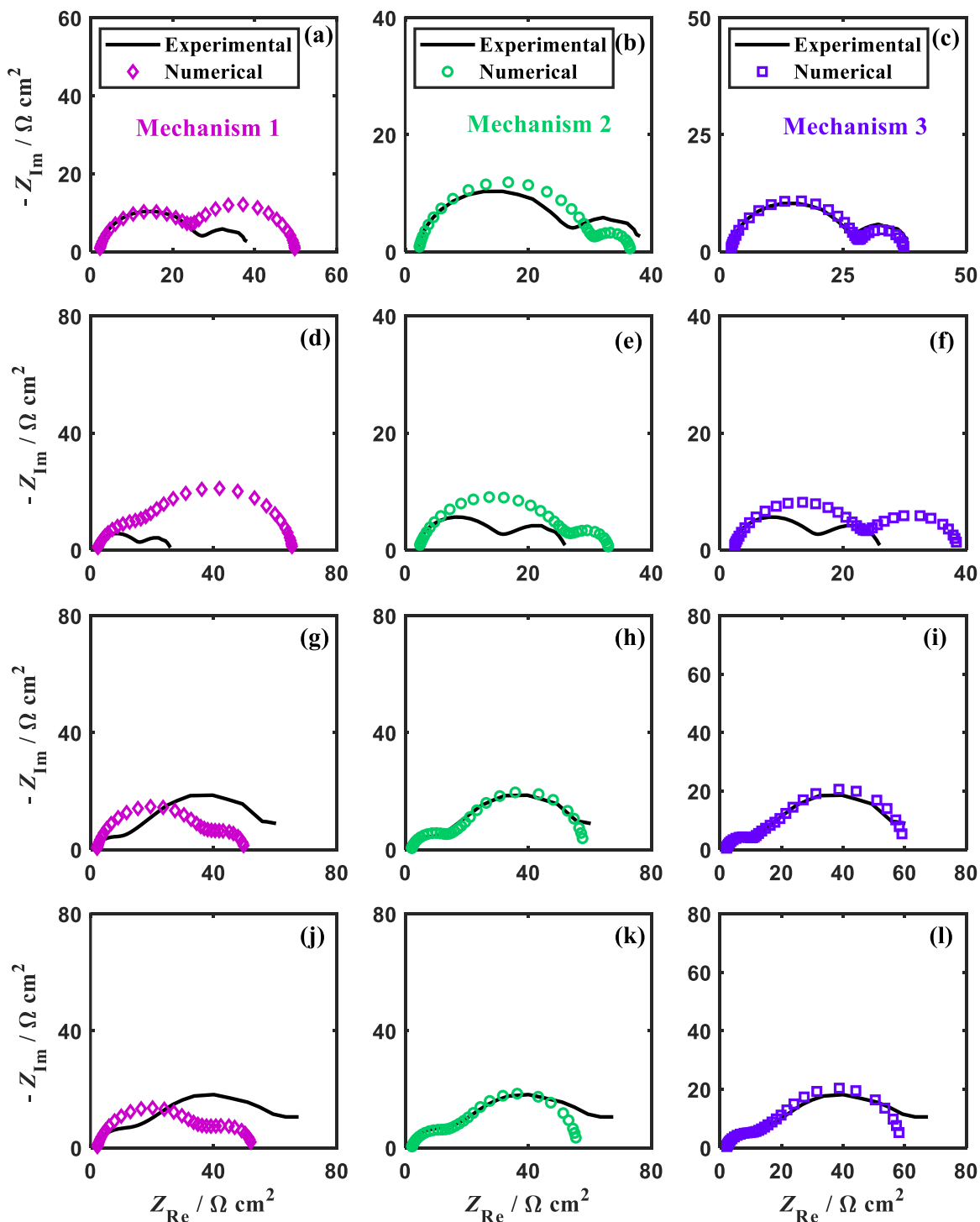


**Figure 3.** Complex plane plot of experimental (—) and simulated impedance data. Three reaction mechanisms, viz. 1 ( $\diamond$ ), 2 ( $\circ$ ) and 3 ( $\square$ ) were employed in simulations. (a), (b), and (c) represent data at  $E_{dc} = -0.1$  (V vs. OCP) with  $E_{ac0} = 0.02$  V using mechanism 1, 2 and 3 resp.; (d), (e), and (f) represent data at  $E_{dc} = -0.1$  (V vs. OCP) with  $E_{ac0} = 0.1$  V using mechanism 1, 2 and 3 resp.; (g), (h), and (i) represent data at  $E_{dc} = -0.3$  (V vs. OCP) with  $E_{ac0} = 0.02$  V using mechanism 1, 2 and 3 resp.; and, (j), (k), and (l) represents data at  $E_{dc} = -0.3$  (V vs. OCP) with  $E_{ac0} = 0.1$  V using 1, 2 and 3 resp. The optimized parameters used in the simulations are listed in Table 1 (see EIS fitting column).

A comparison of the experimental and model results in Figs. 3 (b, c, e, and f) shows that the key features of EIS data, at -0.1 (V vs OCP) dc potential, are captured to more or less the same extent by the two models, namely mechanism 2 and 3. The simulated data shows that the charge transfer resistance ( $R_{ct}$ ) and polarization resistance ( $R_p$ ) values decrease with an increase in perturbation amplitude at -0.1 (V vs OCP) dc bias, and this matches the trend seen in the experimental data. A comparison of the results in Fig. 3 (h, i, k, and l) shows that at a dc bias -0.3 (V vs OCP), the predictions of reaction mechanisms 2 and 3 are closer to the experimental results compared to the predictions of mechanism 1. For mechanism 2, the model predicted data also show that the  $R_{ct}$  and  $R_p$  values remained more or less the same with an increase in perturbation amplitude at this dc bias. Although the match between the experimental data and the data simulated with mechanism 2 is not exact (Figs. 3b, 3e, 3h, and 3k), it is semi-quantitative. The RSS values obtained after the optimization are used to calculate AIC scores for the three models and are listed in the last two rows of Table 1. These results suggest that model 1 can be eliminated easily, and it also suggests that model 2, i.e., the reaction mechanism involving  $\text{Cu}_{\text{ads}}^{1+}$  as intermediate species, is a slightly better choice than mechanism 3.

#### 4.3.2 Higher harmonics current

To fit the model to the experimental data at fundamental as well as higher harmonics, the following methodology was employed. Current values predicted by the model were grouped as fundamental, 2<sup>nd</sup> and 3<sup>rd</sup> harmonic, and complex current values were used for comparison. The optimum parameters were found by minimizing the RSS values as convergence criteria,

$$\text{RSS} = \sum_{j=1}^M \left[ \sum_{k=1}^N \left( \sum_{l=1}^O \left| \frac{i_{\text{Exp}}(j,k,l) - i_{\text{Model}}(j,k,l)}{i_{\text{Exp}}(j,k,l)} \right|^2 \right) \right] \quad (9)$$

Here  $M$  is the total number of operating conditions ( $E_{dc}$  and  $E_{ac0}$  pair),  $N$  is the total number of harmonics analyzed, and  $O$  is the total number of frequencies at which data were acquired.  $i_{\text{Exp}}(j,k,l)$  and  $i_{\text{Model}}(j,k,l)$  are the experimental and model-predicted  $k^{\text{th}}$  harmonic complex current data at  $l^{\text{th}}$  frequency and at  $j^{\text{th}}$  operating condition. Although analyses were performed at all four conditions for the three candidate reaction mechanisms, only a few selected results of reaction mechanisms 2, specifically, results in mixed control regime ( $E_{dc} = -0.3$  V vs OCP), are described here. It is to be noted that the estimation of RSS using other weight factors, such as unity weight factor, yielded essentially the same results.

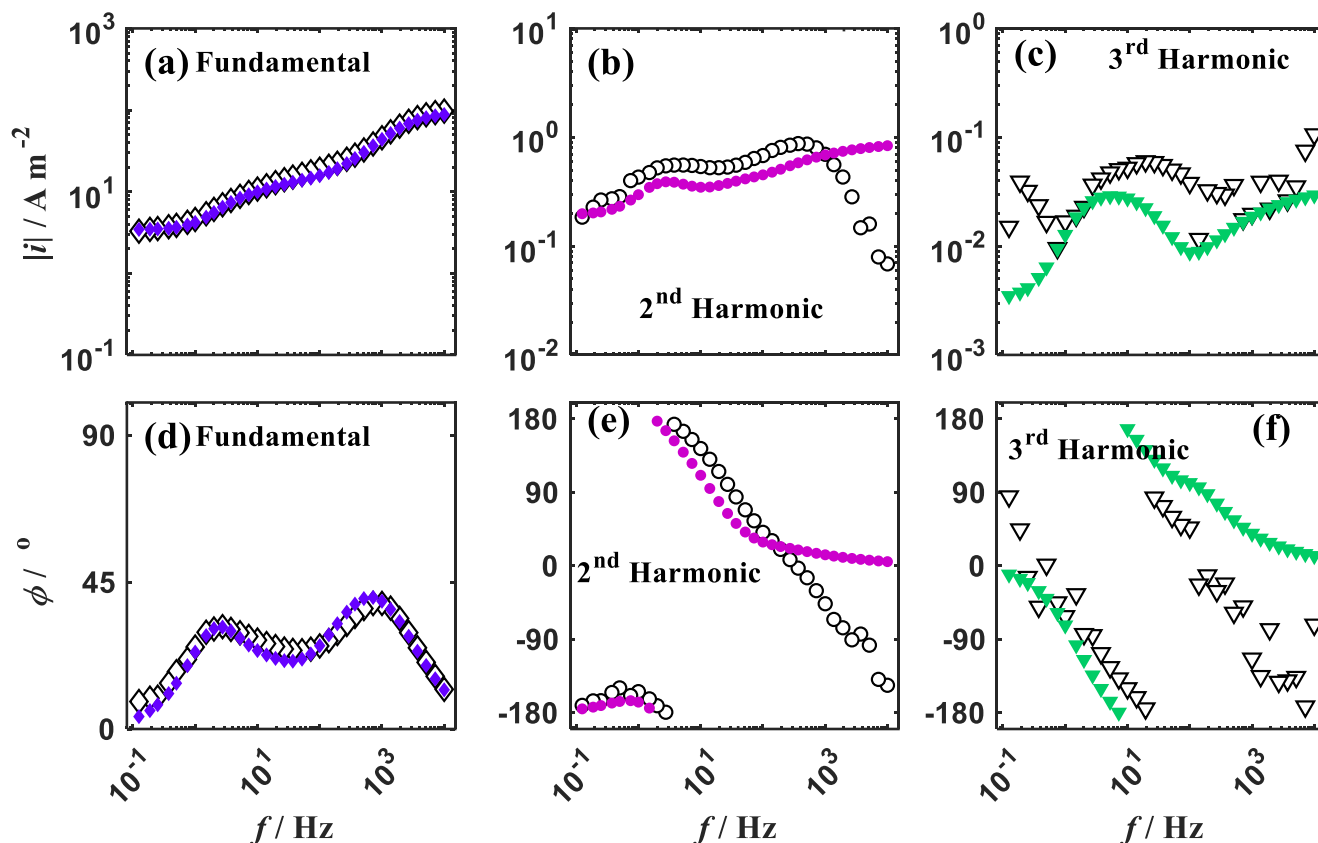


**Figure 4.** Bode plots of NLEIS results, experimental (open markers) and numerical simulations (filled markers) using reaction mechanism 2, obtained at 0.02 V perturbation amplitude over  $E_{dc} = -0.3$  V vs OCP. The optimized parameters used in the simulation are given in Table 2. Fundamental ( $\diamond$ ,  $\blacklozenge$  - simulated data without accounting  $R_{sol}$ ,  $\blacktriangleright$  - current data accounting for  $R_{sol}$  at fundamental alone): (a) magnitude and (d) phase; Second harmonic ( $\circ$ ,  $\bullet$ ): (b) magnitude and (e) phase; and, Third harmonic ( $\nabla$ ,  $\blacktriangledown$ ): (c) magnitude and (f) phase.

Figure 4 shows the experimental and simulated harmonic currents predicted by model 2 at  $E_{ac0} = 0.02$  V and  $E_{dc} = -0.3$  (V vs OCP) as Bode plots. The simulated results are represented by filled markers, while the experimental results are shown as open markers. The presence of higher harmonics indicates that the system has already started deviating from the linear conditions at an amplitude perturbation of 20 mV. A comparison of the experimental and model results corrected for solution resistance at fundamental (Figs. 4a and 4d) shows that the model predictions match the experimental results at most of the frequencies. Fig. 4b shows that the 2<sup>nd</sup> harmonic magnitude and phase are predicted well by the model in the mid and low-frequency range, but at high frequencies, the model predicted values significantly larger than the experimental data. This can be attributed to solution resistance which is not accounted for in the simulations. Figure 4c shows that the third harmonic magnitude as predicted by simulations is consistently lower than the measured values, but the trend in magnitude vs frequency is captured well in the mid-frequency range. The third harmonic experimental data at low and high frequencies are a little noisy due to the low amplitude of perturbation. The simulated phase values (Fig. 4f) match well with experimental values except at high frequencies, which, as discussed earlier, can be attributed to the solution resistance effect.

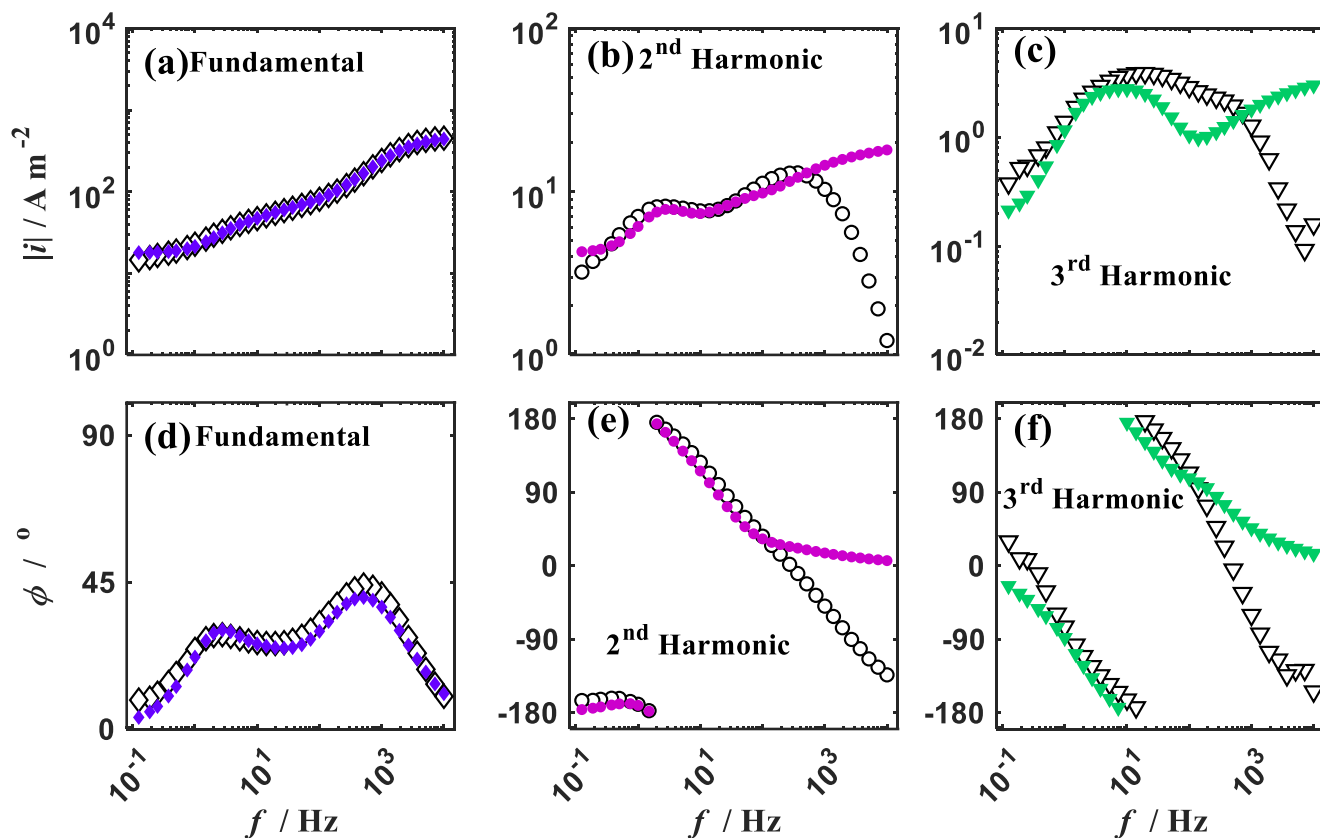


**Figure 5.** Bode plots of NLEIS results, experimental (open markers) and numerical simulations (filled markers) using reaction mechanism 2, obtained at 0.1 V perturbation amplitude over  $E_{dc} = -0.3$  V vs OCP. The optimized parameters used in the simulation are given in Table 2. Fundamental ( $\diamond$ ,  $\blacklozenge$  - simulated data without accounting  $R_{sol}$ ,  $\blacktriangleright$  - current data accounting for  $R_{sol}$  at fundamental alone): (a) magnitude and (d) phase; Second harmonic ( $\circ$ ,  $\bullet$ ): (b) magnitude and (e) phase; and, Third harmonic ( $\nabla$ ,  $\blacktriangledown$ ): (c) magnitude and (f) phase.

Figure 5 shows the Bode plots of experimental harmonic currents obtained at  $E_{ac0} = 100$  mV with dc bias as  $-0.3$  (V vs. OCP) at 900 rpm and simulated data predicted by reaction mechanism 2. Figures 5a and 5d show that the experimental and model data corrected for solution resistance at fundamental match reasonably well at all the frequencies. Figure 5b shows that the model predicted 2<sup>nd</sup> harmonic magnitude match well with the experimental data except at high frequencies. The trends in phase values are also predicted well except in the high-frequency region. In the 3<sup>rd</sup> harmonic magnitude and phase too, the trends are predicted well except at high frequencies (Figs. 5c and 5f). The comparison of NLEIS simulation results of mechanism 2, at  $E_{ac0} = 20$  mV and 100 mV at  $E_{dc} = -0.1$  V vs OCP are not given here, but it was observed that the match between experimental and model-predicted is semi-quantitative. The NLEIS predictions of mechanism 2 do not match the experimental results quantitatively at all operating conditions but concur semi-quantitatively. This could be because of (1) the convection and electromigration effects, which are not modelled, are significant; (2) the optimization process is computationally intensive and global optimum may not have been reached; or, (3) it is also possible that some of the assumptions employed in the model are responsible for the observed differences. The SEM images of the electrode surface after deposition (Fig. 6) clearly show that the actual deposit is made of

small crystallite as against the assumption of monolayer growth employed in the model, and this could contribute to some of the deviations between the model predictions and experimental results.

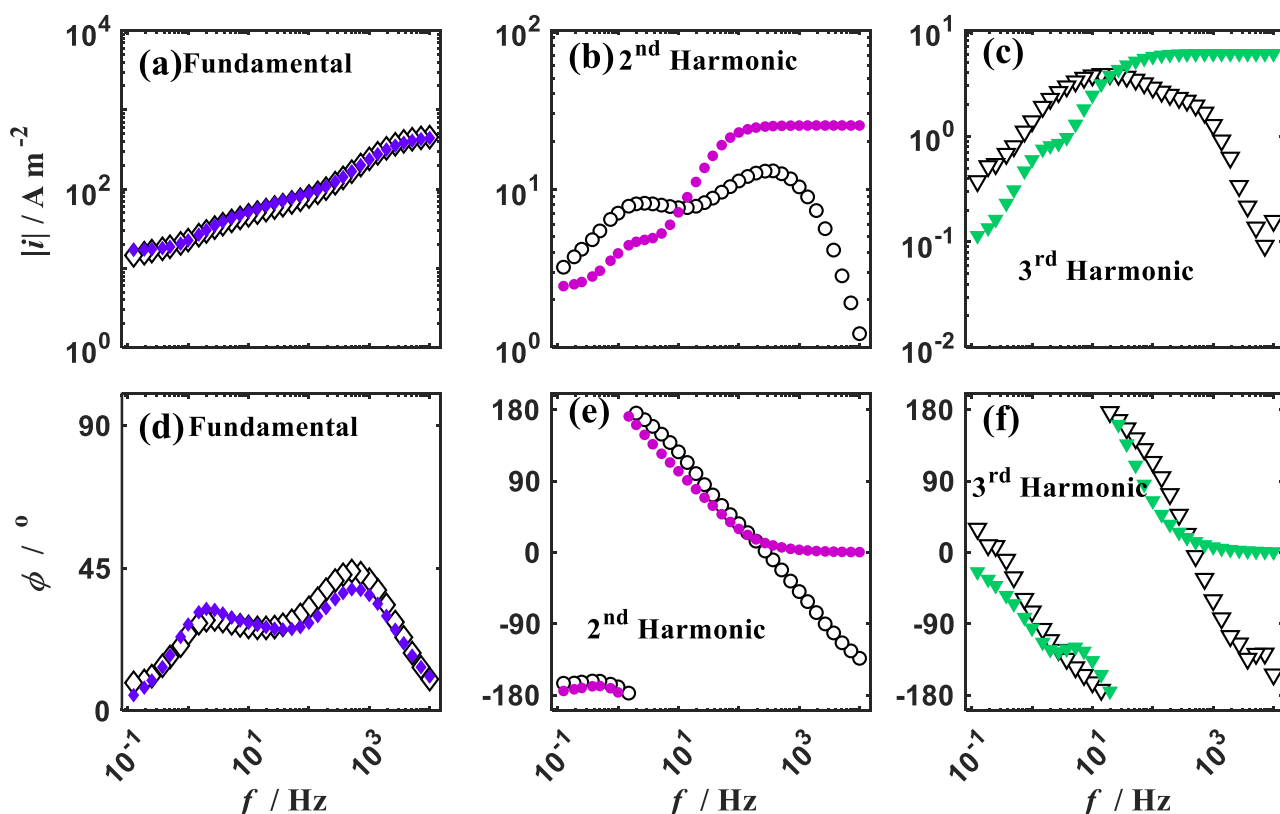


**Figure 6.** Bode plots of NLEIS results, experimental (open markers) and numerical simulations (filled markers) using reaction mechanism 3, obtained at 0.1 V perturbation amplitude over  $E_{dc} = -0.3$  V vs OCP. The optimized parameters used in the simulation are given in Table 2. Fundamental ( $\diamond$ ,  $\blacklozenge$  - simulated data without accounting  $R_{sol}$ ,  $\blacktriangleright$  - current data accounting for  $R_{sol}$  at fundamental alone): (a) magnitude and (d) phase; Second harmonic ( $\circ$ ,  $\bullet$ ): (b) magnitude and (e) phase; and, Third harmonic ( $\nabla$ ,  $\blacktriangledown$ ): (c) magnitude and (f) phase.

The predictions of mechanism 3, for the optimized parameter set given in Table 2, were obtained at four different operating conditions as mentioned earlier. The Fig. 6 shows the experimental as well as model predicted data at one condition i.e.,  $E_{dc} = -0.3$  V vs. OCP and  $E_{ac0} = 100$  mV. As we can see from the figure, the results at higher harmonics had a poor match between experimental and simulated data. The AIC scores calculated using the final RSS values are listed in the last two rows of Table 2. AIC is an estimator of the relative quality of the model for a given data. Among the three mechanisms evaluated in this work, the AIC score of mechanism 2 is the least and hence mechanism 2 was employed to predict the concentration and fractional surface coverage trends. While the match between the NLEIS model predictions and experimental values are not very good, it is to be noted that, for a complex system, modelling NLEIS response at multiple frequencies, ac perturbation values, and dc bias, while ensuring that polarization data are also predicted reasonably well, is very challenging. Literature [9, 10, 13] also shows that the match is usually qualitative or semi-quantitative.

**Table 2.** Optimized parameters from the least-square fitting of complex currents up to third harmonics at four different conditions ( $E_{ac0} = 0.02$  V and 0.1 V perturbed over - 0.1 (V vs OCP) and -0.3 (V vs OCP)) along with potentiodynamic polarization data at 4 different rpms, viz. 100, 400, 900, and 1600. The corresponding RSS and AIC values are listed in the last two rows.

Parameters	Model 2	Model 3
$k_{10}$ (Cm s <sup>-1</sup> )	$1.5 \times 10^{-2}$	$9.73 \times 10^{-2}$
$k_{-10}$ (Mol cm <sup>-2</sup> s <sup>-1</sup> )	$9.9 \times 10^{-9}$	$1.9 \times 10^{-6}$
$\alpha_1$	0.319	0.2
$k_{20}$ (Mol cm <sup>-2</sup> s <sup>-1</sup> )	$2.21 \times 10^{-8}$	$3.7 \times 10^{-8}$
$b_2$ (V <sup>-1</sup> )	--	--
$k_{-20}$ (Mol cm <sup>-2</sup> s <sup>-1</sup> )	--	$3.6 \times 10^{-9}$
$b_{-2}$ (V <sup>-1</sup> )	--	--
$\alpha_2$	0.153	0.44
$k_{30}$ (Mol cm <sup>-2</sup> s <sup>-1</sup> )	--	$6.9 \times 10^{-9}$
$\Gamma$ (Mol cm <sup>-2</sup> )	$4.39 \times 10^{-10}$	$5.86 \times 10^{-9}$
RSS	15	23
AIC	<b>-435</b>	<b>-369</b>

#### 4.4. Surface Characterization

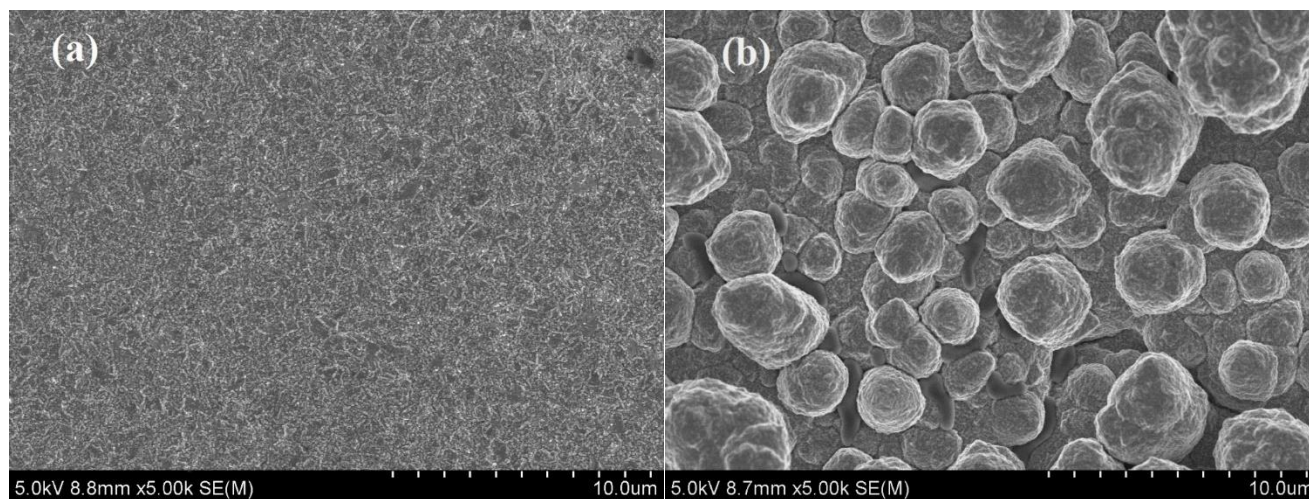


**Figure 7.** Scanning electron micrographs of Cu electrode after acquiring NLEIS data in a solution with 10 mM CuSO<sub>4</sub> and 10 mM H<sub>2</sub>SO<sub>4</sub>, and 1 M NaClO<sub>4</sub> as supporting electrolyte, (a)  $E_{dc} = -0.1$  (V vs. OCP) and  $E_{ac0} = 0.1$  V; and, (b)  $E_{dc} = -0.3$  (V vs. OCP) and  $E_{ac0} = 0.1$  V.

The scanning electron microscopy (SEM) image of Cu electrode surface after acquiring NLEIS data at a dc potential of -0.1 (V vs OCP), with 0.1 V ac perturbation amplitude ( $E_{ac0}$ ), is given in Fig. 7a. The solution contained 10 mM CuSO<sub>4</sub> and 10 mM H<sub>2</sub>SO<sub>4</sub>, and 1 M NaClO<sub>4</sub> as supporting electrolytes, and the duration of the experiment was ~ 30 min. The deposits are small crystals of sub-

micron dimensions and are randomly distributed. On the other hand, when a larger cathodic potential of -0.3 (V vs OCP) was applied along with an ac perturbation of 0.1 V amplitude, the results (Fig. 7b) show that the deposits form sub-micron poly-crystals but with a flower-like pattern. The SEM images of electrode surface after deposition (Fig. 7) clearly show that the actual deposit is made of small crystallite as against the assumption of monolayer growth employed in the model, and this could contribute to some of the deviations between the model predictions and experimental results.

## 5. CONCLUSIONS

Cu electrodeposition process was investigated using potentiodynamic polarization and NLEIS techniques. Three candidate reaction mechanisms were evaluated, and the governing equations were solved employing a direct numerical integration while accounting for the mass transfer effect by diffusion. The optimum parameter values were obtained by simultaneously fitting the model predicted values of PDP and fundamental as well as higher harmonic currents to the corresponding experimental data using the RSS value as convergence criteria. Multi-polarization data predicted by three reaction mechanisms match the experimental data well. However, NLEIS results along with PDP show that among the three mechanisms evaluated, reaction mechanism 2 yields the lowest AIC score and offers a better description of Cu electrodeposition. NLEIS technique has the potential to differentiate reaction mechanism models that yield similar polarization and impedance data but differ in their higher harmonics response.

## ACKNOWLEDGMENT

Author thanks Prof. S Ramanathan, Department of Chemical Engineering, Indian Institute of Technology Madras, India, for the valuable discussions and correcting the manuscript. The author gratefully acknowledges financial support by the Department of Science and Technology, Ministry of Science and Technology, India, under an extramural research funding scheme (grant no. SB/S3/CE/041/2015).

## CONFLICTS OF INTEREST

The author declares that there are no known conflicts of interest associated with this publication.

## APPENDIX A

### (a). Steps involved in polarization data simulation

- (i)  $k_{-20}$  is calculated using the equation  $k_{-20} = \frac{k_{10}k_{20}C_{\text{bulk}}}{k_{-10}}$
- (ii) The potential  $E$  is set to  $E_{\text{dc}}$ , and the rate constants are calculated as  $k_{j\text{dc}} = k_{j0}e^{b_j E_{\text{dc}}}$  ( $j = 1, -1, 2$  and  $-2$ )
- (iii) Since the potential is constant ( $E = E_{\text{dc}}$ ), under steady-state conditions, Eq. (3) in manuscript is set to zero,  $k_{1\text{dc}}(1 - \theta_{1+,ss})C_{0,ss} - k_{-1\text{dc}}\theta_{1+,ss} - k_{2\text{dc}}\theta_{1+,ss} + k_{-2\text{dc}}(1 - \theta_{1+,ss}) = 0$ . Here, subscript 'SS' denotes

steady-state conditions, and  $C_{0,ss}$  is the steady state concentration of  $\text{Cu}_{\text{sol}}^{1+}$  at the electrode-

electrolyte interface. This, upon re-arrangement yields,  $\theta_{1+,ss} = \frac{k_{1dc}C_{0,ss} + k_{-2dc}}{k_{1dc}C_{0,ss} + k_{-1dc} + k_{2dc} + k_{-2dc}}$  (A1)

(iv) Under steady-state conditions, Eq. (4) of the manuscript is also set to zero,

$$\frac{\partial C(x,t)}{\partial t} = D \frac{\partial^2 C(x,t)}{\partial x^2} = 0. \text{ Applying the boundary conditions } C(x=0) = C_{0,ss} \text{ and } C(x=\delta) = C_{\text{bulk}},$$

$$\text{we get, } C(x) = C_{0,ss} + \frac{x}{\delta}(C_{\text{bulk}} - C_{0,ss}) \text{ and } \frac{\partial C}{\partial x} = \frac{(C_{\text{bulk}} - C_{0,ss})}{\delta}. \quad (\text{A2})$$

Substituting  $\frac{\partial C}{\partial x} = \frac{(C_{\text{bulk}} - C_{0,ss})}{\delta}$  in Eq. (5) of the manuscript under steady state condition,

$$D \frac{\partial C}{\partial x} = D \frac{(C_{\text{bulk}} - C_{0,ss})}{\delta} = k_{1dc}(1 - \theta_{1+,ss})C_{0,ss} - k_{-1dc}\theta_{1+,ss}.$$

Under steady state condition,  $k_{1dc}(1 - \theta_{1+,ss})C_{0,ss} - k_{-1dc}\theta_{1+,ss} = k_{2dc}\theta_{1+,ss} - k_{-2dc}(1 - \theta_{1+,ss})$ . After substituting it in the above equation and re-arranging, we get

$$C_{0,ss} = C_{\text{bulk}} - \frac{\delta}{D}[k_{2dc}\theta_{1+,ss} - k_{-2dc}(1 - \theta_{1+,ss})] \quad (\text{A3})$$

(v) After substituting Eq. (A3) in Eq. (A1) and re-arranging, we get a quadratic equation in  $\theta_{1+,ss}$ ,

$$A_1\theta_{1+,ss}^2 + B_1\theta_{1+,ss} + G_1 = 0, \text{ whose solution is } \theta_{1+,ss} = \frac{-B_1 - \sqrt{B_1^2 - 4A_1G_1}}{2A_1} \quad (\text{A4})$$

the other solution is neglected since it estimates  $\theta_{1+,ss} > 1$ .

$$\text{Here, } A_1 = \frac{\delta}{D}k_{1dc}(k_{2dc} + k_{-2dc}); B_1 = -\frac{\delta}{D}k_{1dc}(k_{2dc} + 2k_{-2dc}) - (k_{-1dc} + k_{2dc} + k_{-2dc}) - k_{1dc}C_{\text{bulk}}$$

$$G_1 = k_{1dc}C_{\text{bulk}} + \frac{\delta}{D}k_{1dc}k_{-2dc} + k_{-2dc}$$

(vi) Substituting Eq. (A4) in Eq. (A3) the steady-state concentration  $C_{0,ss}$  is calculated. The steady-state current is calculated by substituting Eq. (A4) in Eq. (A5)

$$i_F = F[k_{1dc}(1 - \theta_{1+,ss})C_{0,ss} - k_{-1dc}\theta_{1+,ss} + k_{2dc}\theta_{1+,ss} - k_{-2dc}(1 - \theta_{1+,ss})] \quad (\text{A5})$$

(b). The steps involved in NLEIS data simulation

(i) The boundary layer was discretized into 'N' points, with point 1 as surface and N as bulk.

(ii) Using the finite difference method, we can write the right side of the Eq. (4) of the manuscript as shown below,

$$1) \text{ At } x = 0, \text{ i.e. } j = 1, \left. \frac{\partial^2 C}{\partial x^2} \right|_{j=1} = \frac{\left. \frac{\partial C}{\partial x} \right|_{j=2} - \left. \frac{\partial C}{\partial x} \right|_{j=1}}{\Delta x}$$

$$\text{From Eq. (5) of manuscript, } \left. \frac{\partial C}{\partial x} \right|_{j=1} = \frac{1}{D}[k_1(1 - \theta_{1+})C_1 - k_{-1}\theta_{1+}] \text{ and } \left. \frac{\partial C}{\partial x} \right|_{j=2} = \frac{C_3 - C_2}{\Delta x}$$

Hence, we can write,  $\left. \frac{dC}{dt} \right|_{j=1} = D \frac{(C_3 - C_2)}{(\Delta x)^2} - \frac{1}{(\Delta x)} (k_1(1 - \theta_{1+})C_1 - k_{-1}\theta_{1+})$

2) For all points and except 1 and  $N$ ,  $\frac{dC_j}{dt} = D \frac{C_{j+1} + C_{j-1} - 2C_j}{(\Delta x)^2}$

3) At  $j = N$ ,  $C_N = C_{A\text{-bulk}}$

(iii) All the equations are converted to non-dimensional form using the following dimensionless variables ( $\bar{x}$  - position;  $\bar{t}$  - time;  $\bar{C}_j$  - concentration;  $\bar{k}_j$  - rate constant; and,  $\bar{\Gamma}$  - total number of sites).

$$\bar{x} = \frac{x}{\delta}, \bar{t} = \frac{D}{\delta^2} t, \bar{C}_j = \frac{C_j}{C_{\text{bulk}}}, \bar{k}_1 = \frac{k_1 \delta}{D} \text{ and } \bar{k}_j = \frac{k_j \delta}{DC_{\text{bulk}}}, j = -1, 2 \text{ \& } -2, \text{ and } \bar{\Gamma} = \frac{\Gamma}{C_{\text{bulk}} \delta} \quad (\text{A6})$$

(iv) The overall differential equation can be written in a non-dimensional form as,

$$\frac{d}{dt} \begin{bmatrix} \bar{C}_1 \\ \bar{C}_2 \\ \vdots \\ \bar{C}_j \\ \vdots \\ \bar{C}_N \\ \theta_{1+} \end{bmatrix} = \begin{bmatrix} \frac{\bar{C}_3 - \bar{C}_2}{(\Delta x)^2} - \frac{1}{\Delta x} [\bar{k}_1(1 - \theta_{1+})\bar{C}_1 - \bar{k}_{-1}\theta_{1+}] \\ \frac{\bar{C}_3 - 2\bar{C}_2 + \bar{C}_1}{\Delta x^2} \\ \vdots \\ \frac{\bar{C}_{j+1} - 2\bar{C}_j + \bar{C}_{j-1}}{\Delta x^2} \\ \vdots \\ 0 \\ \frac{1}{\bar{\Gamma}} [\bar{k}_1(1 - \theta_{1+})\bar{C}_1 - \bar{k}_{-1}\theta_{1+} - \bar{k}_2\theta_{1+} + \bar{k}_{-2}(1 - \theta_{1+})] \end{bmatrix} \quad (\text{A7})$$

(v) The steady-state solution,  $\theta_{1+,ss}$  and  $C_{1,ss}$ , are used as the initial values to integrate Eq. (A7).

(vi) Integration was done using *ode15s* in Matlab®. Initially, integration was done until a certain wait time to get steady periodic values. The resulting non-dimensional surface concentration was used as initial values for further integration.

(vii) After the signal is steady periodic, 10 loops are analyzed and unsteady state current was calculated using the surface concentration and fractional surface coverage area obtained from integration.

$$i_F(t) = F [k_1(1 - \theta_{1+})C_1 - k_{-1}\theta_{1+} + k_2\theta_{1+} - k_{-2}(1 - \theta_{1+})] \quad (\text{A8})$$

(viii) This unsteady state current was subjected to FFT and current magnitude and phase were extracted up to third harmonics, *i.e.*, the time series data in Eq. (A8) was subjected to FFT, to obtain the values of  $i_0, i_1, i_2 \dots$  and  $\phi_1, \phi_2 \dots$  in the following equation (Eq. (A9))

$$i_F(t) = i_0 + i_1 \sin(\omega t + \phi_1) + i_2 \sin(2\omega t + \phi_2) + \dots \quad (\text{A9})$$

(ix) The current components are plotted as a function of frequency, *i.e.*, NLEIS results as Bode plot.

(x) We have modeled the double layer as a constant phase element and the capacitive current was calculated as follows. Capacitive current,  $i_C = \frac{1}{Q(\omega j)^n}$ ,  $Q$  is the CPE parameter and  $n$  is the CPE

exponent, obtained from EEC fitting of EIS data (from 9.984 kHz to 0.125 Hz) to R(Q(RO)) circuit using Zsimpwin® commercial software.

## References

1. D.D. Macdonald, *Electrochim. Acta*, 35 (1990) 1509.
2. A. Lasia, *Electrochemical Impedance Spectroscopy and its Applications*, Springer, (2014) New York.
3. M.E. Orazem, B. Tribollet, *Electrochemical impedance spectroscopy*, John Wiley & Sons, (2011) New Jersey.
4. W. Cheng, S. Luo, Y. Chen, *Int J Electrochem Sci*, 14 (2019) 4254.
5. M. Brza, S.B. Aziz, H. Anuar, F. Ali, R.T. Abdulwahid, J.M. Hadi, *Int. J. Electrochem. Sci.*, 16 (2021) Article ID: 210639.
6. N. Harting, N. Wolff, U.F. Roder, U. Krewer, *J. Electrochem. Soc.*, 166 (2019) A277.
7. M.D. Murbach, D.T. Schwartz, *J. Electrochem. Soc.*, 164 (2017) E3311.
8. R. Pachimatla, M. Thomas, O.C. Sameer Rahman, R. Srinivasan, *J. Electrochem. Soc.*, 166 (2019) H304.
9. T. Kadyk, R. Hanke-Rauschenbach, K. Sundmacher, *Int. J. Hydrogen Energy*, 37 (2012) 7689.
10. J.R. Wilson, D.T. Schwartz, S.B. Adler, *Electrochim. Acta*, 51 (2006) 1389.
11. N. Wolff, N. Harting, M. Heinrich, U. Krewer, *Electrochim. Acta*, 298 (2019) 788.
12. F. Fasmin, R. Srinivasan, *J. Electrochem. Soc.*, 164 (2017) H443.
13. N. Xu, D.J. Riley, *Electrochim. Acta*, 94 (2013) 206.
14. N. Xu, J. Riley, *Electrochem. Commun.*, 13 (2011) 1077.
15. K. Darowicki, *Electrochim. Acta*, 40 (1995) 439.
16. D.K. Wong, D.R. MacFarlane, *J. Phys. Chem.*, 99 (1995) 2134.
17. V.V. Panic, T.R. Vidakovic-Koch, M. Andric, M. Petkovska, K. Sundmacher, *J. Phys. Chem. C*, 115 (2011) 17352.
18. T.R. Vidakovic-Koch, V.V. Panic, M. Andric, M. Petkovska, K. Sundmacher, *J. Phys. Chem. C*, 115 (2011) 17341.
19. D.A. Harrington, *Can. J. Chem.*, 75 (1997) 1508.
20. B. Bensmann, M. Petkovska, T. Vidakovic-Koch, R. Hanke-Rauschenbach, K. Sundmacher, *J. Electrochem. Soc.*, 157 (2010) B1279.
21. S.N. Victoria, S. Ramanathan, *Electrochim. Acta*, 56 (2011) 2606.
22. S. Santhanam, V. Ramani, R. Srinivasan, *J. Solid State Electrochem.*, 16 (2012) 1019.
23. N.S. Kaisare, V. Ramani, K. Pushpavanam, S. Ramanathan, *Electrochim. Acta*, 56 (2011) 7467.
24. F. Fasmin, R. Srinivasan, *J. Solid State Electrochem.*, 19 (2015) 1833.
25. J.M. Bockris, M. Enyo, *Trans. Faraday Soc.*, 58 (1962) 1187.
26. D. Barkey, F. Oberholtzer, Q. Wu, *J. Electrochem. Soc.*, 145 (1998) 590.
27. S. Wu, Z. Yin, Q. He, G. Lu, Q. Yan, H. Zhang, *J. Phys. Chem. C*, 115 (2011) 15973.
28. S. Krzewska, *Electrochim. Acta*, 42 (1997) 3531.
29. J.J. Kelly, A.C. West, *J. Electrochem. Soc.*, 145 (1998) 3477.
30. C. Gabrielli, P. Mocoteguy, H. Perrot, R. Wiart, *J. Electroanal. Chem.*, 572 (2004) 367.
31. W. Shao, G. Pattanaik, G. Zangari, *J. Electrochem. Soc.*, 154 (2007) D201.
32. M.H. Garrido, M. Pritzker, *J. Electroanal. Chem.*, 594 (2006) 118.
33. R.P. Venkatesh, S. Ramanathan, *J. Solid State Electrochem.*, 14 (2010) 2057.
34. D. Harrington, B. Conway, *Electrochim. Acta*, 32 (1987) 1703.
35. A. Lasia, A. Rami, *J. Electroanal. Chem. Interfacial Electrochem.*, 294 (1990) 123.
36. R. Pachimatla, R. Srinivasan, *ECS Trans.*, 85 (2018) 1145.
37. M. Amrutha, R. Srinivasan, *J. Solid State Electrochem.*, 21 (2017) 91.
38. J. Prong, T. Jaszay, A. Caprani, J. Frayret, *J. Appl. Electrochem.*, 25 (1995) 1031.

39. M. Ingdal, R. Johnsen, D.A. Harrington, *Electrochim. Acta*, 317 (2019) 648

© 2022 The Authors. Published by ESG ([www.electrochemsci.org](http://www.electrochemsci.org)). This article is an open access article distributed under the terms and conditions of the Creative Commons Attribution license (<http://creativecommons.org/licenses/by/4.0/>).